electronics

MDPI

Article

A Multiple-Input Multiple-Output Antenna with Metamaterial Enhancement for 5G Channel Sounding in the Upper 6 GHz Band

Adnane Ghiat [1], Jesús R. Pérez [2,*], Rafael P. Torres [2], Abdelwahed Tribak [1] and Jaouad Terhzaz [3]

[1] Department of Microwave and Communication Antenna Subsystems, Institute National Des Postes and Telecommunications, INPT, Rabat 10090, Morocco; adnaneghiat@gmail.com (A.G.); tribak@inpt.ac.ma (A.T.)
[2] Departamento de Ingeniería de Comunicaciones, Universidad de Cantabria, 39005 Santander, Spain; rafael.torres@unican.es
[3] Department of Physics, Centre Régional des Métiers de l'Education et de la Formation, CRMEF, Casablanca 20340, Morocco; terhzazj@yahoo.fr
* Correspondence: jesusramon.perez@unican.es

Abstract: This paper presents a compact 2 × 2 multiple-input multiple-output antenna system designed for 5G smartphones operating in the upper 6 GHz band, and which is to be initially considered as a prototype resembling a user terminal in a channel sounding system. The antenna incorporates a split-ring resonator metamaterial layer, enhancing its gain by at least 1.5 dB across the entire bandwidth without increasing the size of the antenna. The results show a good agreement between the simulations and measurements, achieving a strong isolation, below −18 dB; a low envelope correlation coefficient, lower than 0.025; as well as an efficiency exceeding 75%, making it highly suitable for 5G wireless applications, including both indoor as well as outdoor wireless channel characterization.

Keywords: 5G systems; antennas; metamaterials; MIMO systems; wireless channel

Academic Editor: Naser Ojaroudi Parchin

Received: 18 February 2025
Revised: 24 March 2025
Accepted: 26 March 2025
Published: 27 March 2025

Citation: Ghiat, A.; Pérez, J.R.; Torres, R.P.; Tribak, A.; Terhzaz, J. A Multiple-Input Multiple-Output Antenna with Metamaterial Enhancement for 5G Channel Sounding in the Upper 6 GHz Band. *Electronics* **2025**, *14*, 1339. https://doi.org/10.3390/electronics14071339

1. Introduction

The advent of fifth-generation (5G) mobile networks has ushered in a new era of wireless communication, characterized by unprecedented data rates, ultra-low latency, and massive connectivity. As the demand for bandwidth continues to surge, the allocation of new frequency bands and the harmonization of the spectrum becomes imperative. In the framework of the World Radio Communication Conference (WRC-23), one of the outcomes identifies the 6425–7125 MHz frequency band for International Mobile Telecommunications (IMT) in most of the countries in International Telecommunication Union (ITU) regions, including technical conditions to protect Earth-to-space fixed satellite services [1]. This frequency range 1 (FR1) band emerges as a promising frontier for high-capacity communications in urban environments, expanding broadband connectivity and supporting advanced mobile services.

This paper presents an innovative 2 × 2 multiple-input multiple-output (MIMO) antenna system designed for 5G smartphones operating in the 6425–7125 MHz frequency band. Our research addresses two critical challenges in modern smartphone design: the integration of compact, efficient antennas into slim device profiles, and the enhancement of antenna gain to mitigate the higher path loss associated with FR1 and millimeter-wave (mmWave) frequencies.

The miniaturization of antenna systems has become increasingly critical due to the rapid expansion of mobile communication technologies [2]. To address the challenges

associated with bandwidth constraints, researchers have investigated the application of artificial dielectrics and magnetic materials, with a particular emphasis on metamaterials (MTMs) [3]. These engineered electromagnetic structures have demonstrated versatility in various applications, including antennas, filters, and polarizers. Notably, MTMs have been utilized as electromagnetic wave (EMW) absorbers to attenuate undesired frequency coupling in radar systems.

While ultra-wideband (UWB) planar antenna research has predominantly focused on omnidirectional designs due to their comprehensive spatial coverage, unidirectional radiation patterns present distinct advantages in terms of their power efficiency and interference mitigation [4,5]. To enhance the gain characteristics of UWB planar antennas, various methodologies have been proposed, including the implementation of single- and multi-layer frequency selective surface (FSS) configurations [6,7]. The utilization of an FSS as a single-layer reflector shares conceptual similarities with partially reflecting surfaces (PRSs) [8,9].

Furthermore, phase gradient metasurfaces have emerged as a promising technique for enhancing radiation gain by engineering wavefront manipulation to achieve focused radiation patterns [10]. Similarly, single-layer electromagnetic bandgap (EBG) surfaces have been investigated for their ability to suppress surface waves and improve gain performance, as demonstrated in [11,12].

The pursuit of enhanced antenna performance has led to significant interest in the integration of artificial magnetic conductors (AMCs) and negative-index metamaterials (NIMs), particularly for application in modern wireless communication systems. For instance, prior studies have demonstrated that incorporating AMCs into dipole antennas can achieve notable gains [13,14]. One study reported a peak radiation gain of 10.96 dBi at 3 GHz [14]. NIMs, on the other hand, represent a class of engineered structures capable of manipulating electromagnetic (EM) waves in unconventional ways by exhibiting simultaneously negative effective permittivity and permeability. This unique property enables EM wave propagation in directions opposite to those observed in natural materials, offering transformative potential for advanced communication technologies such as 5G and 6G networks. Specifically, NIMs are being explored for use in reconfigurable intelligent surfaces (RIS), a technology essential for tackling urban communication challenges such as high path loss, bandwidth constraints, and signal obstruction. RIS, constructed from thin metamaterial layers, can dynamically manipulate signals through reflection or refraction, significantly improving coverage and overall system performance.

Additionally, NIMs have been extensively investigated for antenna design applications, including beam steering, gain enhancement, wavefront shaping, and reconfigurability. Notable advancements include the use of zero-index MTMs to achieve a peak gain of 12.31 dBi at 7.45 GHz [15], double-stacked NIM layers to achieve gains of 6.20 dBi at 10 GHz [16], and split-ring resonator (SRR)-based lenses to enhance gain to 12.7 dBi across 25–31 GHz [17]. Despite these achievements, existing NIM-based designs often suffer from practical limitations, such as their bulky configurations, geometric complexity, multi-layer implementations, and fabrication challenges. Furthermore, scaling single-element designs into array systems and tuning devices for higher frequency bands remain non-trivial tasks.

Bearing in mind the aforementioned challenges, the aims and main contributions of this research can be summarized as follows:

- This work proposes a novel NIM structure specifically designed for FR1 upper 6 GHz band communication systems. The metamaterial layer, imprinted on a thin dielectric substrate and positioned beneath the antenna, is meticulously engineered to exhibit negative effective permittivity and permeability.

- The experimental results demonstrate significant gain enhancement for the proposed antenna array, highlighting its potential to improve signal quality and extend coverage in 5G networks' higher frequency bands.
- Notably, this study represents the first reported use of negative-refractive-index materials to enhance the gain of conventional MIMO antenna arrays, marking a significant advancement in the field of metamaterial-enabled antenna design.
- This work contributes to the ongoing development of 5G smartphone technology by offering a high-performance antenna that addresses the challenges of next-generation wireless communications through advanced materials and design techniques.
- The antenna prototype, along with a radiofrequency (RF) switch and a radio-over-fiber (RoF) link, will be included at the user terminal (UT) side in a channel sounder [18,19], significantly improving both the realism of the measurements and the accuracy of the channel models obtained through extensive measurement campaigns.

The rest of the paper is organized as follows: Section 2 presents the key aspects of the MIMO antenna design, including the details of its role as one of the key elements of the channel sounder to be developed. Section 3 includes the most representative results, comparing both the antenna designed and the resulting prototype, and, finally, Section 4 outlines the main conclusions that can be drawn from this paper.

2. The MIMO Antenna System

2.1. Antenna Design

The main details concerning the design and analysis of a four-element MIMO antenna for mobile communications in the FR1 6425–7125 MHz band are presented in this section. Figure 1 illustrates the geometry and dimensions of the antenna structure, specifically designed by taking into account the possibility of being integrated into a mobile terminal chassis. The antenna elements, symmetrically arranged along the longitudinal edges of the chassis ground, are fabricated on a Rogers RO4003C substrate (relative dielectric constant, ε_r = 3.55, and loss tangent, tanδ = 0.0021) with a thickness of 0.508 mm or 20 mils. Each element occupies an area of 14.8 × 2 mm^2 on the substrate's top layer, while the chassis ground (140 × 70 mm^2 in size) is printed on the bottom layer.

The optimization of all of the design parameters has been carried out using the CST software (2020) to achieve the target center frequency of 6775 MHz. The optimized geometrical data of the antenna can be found summarized in Table 1.

Table 1. Dimensions of the optimized antenna design.

Parameter	Dimension (mm)
Gx	5.5
Gy	8
L	5
Lf	9.8
Lg	9
Ls	4.6
Lv	8
W	2
Wf	0.8
Wg	14.6
Ws	1
Wv	12

The antenna configuration proposed aims to enhance the MIMO capabilities of mobile devices operating in the specified frequency band, and, in addition, the prototype will,

in the future, be developed into a channel sounding system and will contribute to the know-how in terms of creating realistic channel models for MIMO and deploying massive (mMIMO) systems.

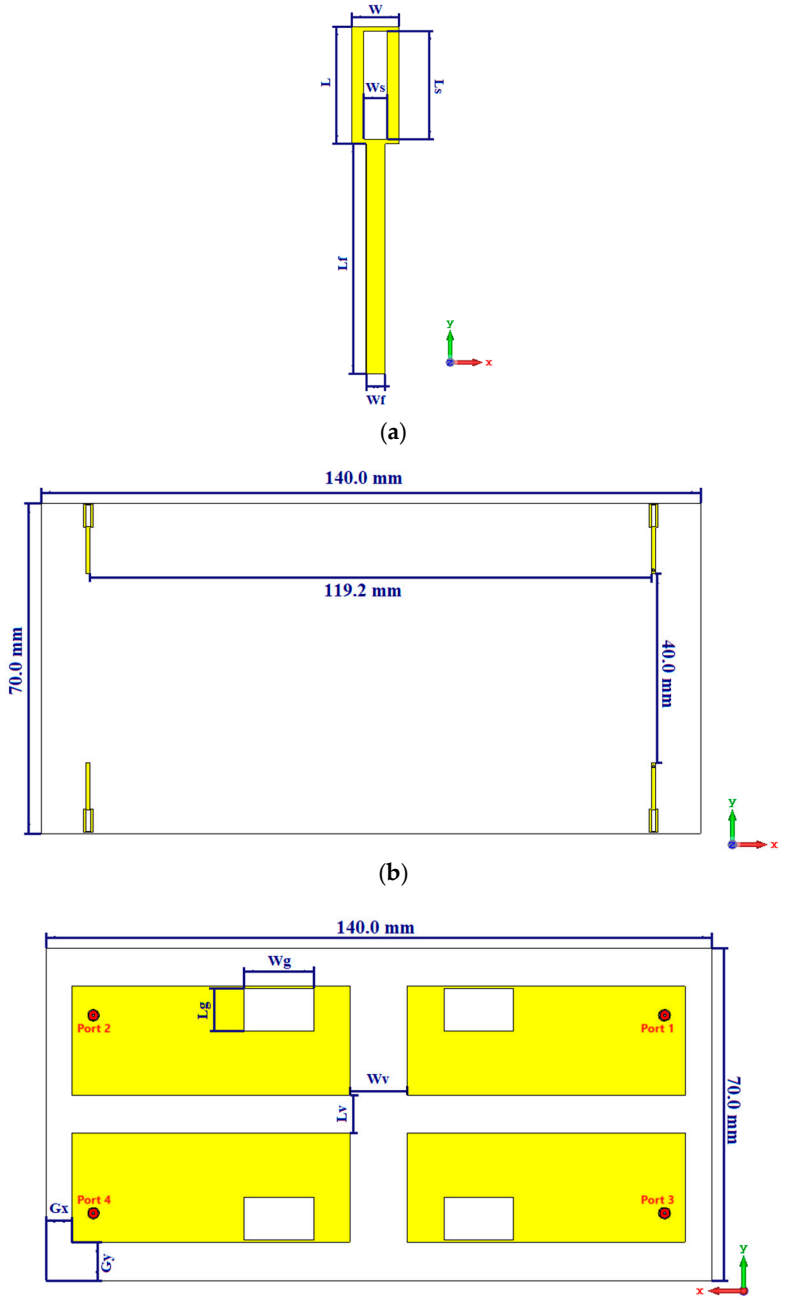

Figure 1. Antenna design: (**a**) single antenna element; (**b**) top view of the 2 × 2 MIMO antenna; (**c**) back view of the MIMO antenna, including the details of the port connections.

2.2. Impact of the Metamaterial-Based Second Layer

The integration of an MTM-based second layer, featuring a concentric ring resonator (CRR) structure, plays a pivotal role in enhancing the performance of MIMO antennas for advanced 5G communication systems. The proposed metamaterial layer, as shown in Figure 2a, employs a CRR structure with a resonant λ_{CRR} = 0.075 λ, and is specifically engineered to exhibit double-negative (DNG) material properties, also referred to as left-handed materials (LHMs). This MTM layer is strategically positioned beneath the MIMO

antenna ground plane already presented in Figure 1c, resulting in the final structure shown in Figure 2b. This way, it creates a complementary electromagnetic interaction that enhances the antenna's radiation characteristics while maintaining the compact form factor required for modern mobile devices. To better elucidate the significance of these properties, Figure 3 provides a graphical representation of the four quadrants defined by the signs of permittivity, ε, and permeability, μ. In this context, the first quadrant corresponds to conventional materials with positive refraction, $\varepsilon > 0$ and $\mu > 0$, enabling forward wave propagation. In contrast, the third quadrant represents DNG materials with negative refraction, $\varepsilon < 0$ and $\mu < 0$, which support backward wave propagation and offer unique wave manipulation capabilities. Notably, the second and fourth quadrants correspond to non-propagating materials due to the combination of $\varepsilon > 0$ and $\mu < 0$ or $\varepsilon < 0$ and $\mu > 0$, resulting in imaginary wave vectors that do not permit electromagnetic wave propagation. The placement of the MTM layer in the third quadrant confirms its suitability for enabling negative refraction and backward wave propagation.

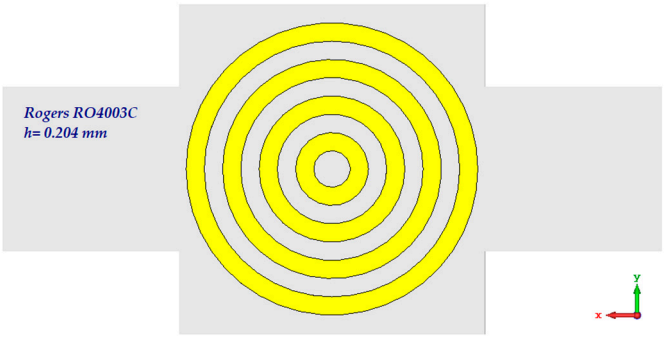

(**a**)

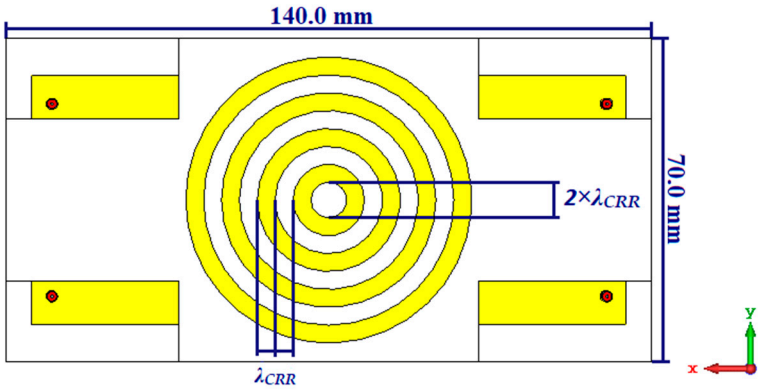

(**b**)

Figure 2. Details of the proposed CRR-based MTM structure: (**a**) topology of the MTM layer; (**b**) back view of the 2 × 2 MIMO antenna with the MTM placed on top of the structure already presented in Figure 1c.

To validate the effectiveness of the proposed MTM structure, simulations were conducted using CST Microwave Studio Suite (2020) under appropriate boundary conditions [20,21]. The scattering parameters S_{11} and S_{21} were analyzed to extract the effective permittivity, ε_{eff}, and permeability, μ_{eff}, using (1)–(4) [20,21] derived from the *S*-parameter matrix:

$$n_{eff} = \frac{1}{kd}\cos^{-1}\left[\frac{1}{2S_{21}}\left(1 - S_{11}^2 + S_{21}^2\right)\right], \quad (1)$$

$$Z = \sqrt{\frac{(1+S_{11})^2 - S_{21}^2}{(1-S_{11})^2 - S_{21}^2}}, \tag{2}$$

$$\varepsilon_{eff} = \frac{n_{eff}}{Z}, \tag{3}$$

$$\mu_{eff} = n_{eff}\, Z, \tag{4}$$

where k is the propagation constant, d is the material thickness, and Z represents the characteristic impedance of the MTM layer.

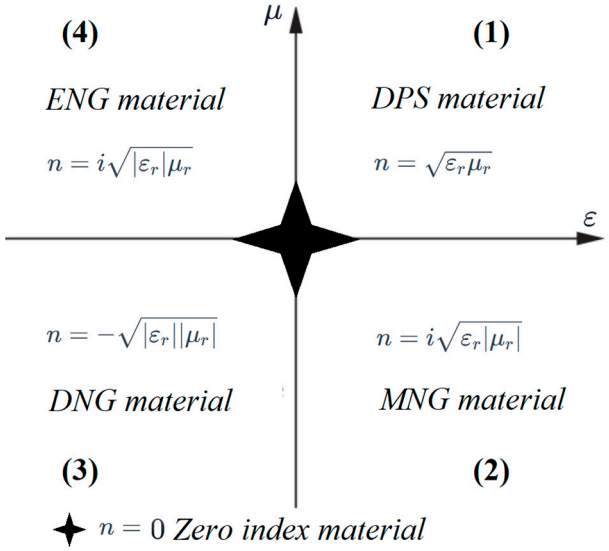

Figure 3. Materials according to the combinations of ε and μ.

As illustrated in Figure 4, the values obtained confirm that both the real parts of permittivity, Re (ε_{eff}), and permeability, Re (μ_{eff}), are negative across the entire 6.4–7.1 GHz range, validating the DNG behavior.

The negative refractive index, n_{eff}, fundamentally alters the propagation characteristics of electromagnetic waves, impacting key factors such as phase velocity and wavefront curvature. In DNG materials, the phase velocity (v_{ph}) is directed opposite to the energy flow, leading to unique wave manipulation capabilities. This behavior facilitates more efficient constructive interference in the far-field region, thereby enhancing gain and improving directivity. Furthermore, the negative refractive index enables precise control over wavefront curvature, making it ideal for the advanced beamforming techniques required in 5G applications, such as dynamic beam steering and spatial multiplexing.

The complex nature of the extracted parameters highlights the energy dissipation characteristics of the MTM layer. The positive imaginary part of permeability (Im (μ_{eff}) > 0), which remains close to zero, indicates the minimal magnetic losses, ensuring high efficiency. Conversely, the negative imaginary part of permittivity (Im(ε_{eff}) < 0) reflects the dielectric losses inherent to the material, providing an optimal balance between absorption and dissipation. This balance is crucial for maintaining high radiation efficiency while minimizing unwanted signal attenuation. These complex constitutive parameters fundamentally adhere to the Kramers–Kronig relations, which establish a mathematical connection between the real and imaginary components of both μ_{eff} and ε_{eff}, confirming that the material response is causal and physically realizable in accordance with electromagnetic theory. This causality principle ensures that the measured electromagnetic response of the MTM structure represents a physically valid system where dispersion and loss mechanisms are interconnected through these fundamental relationships.

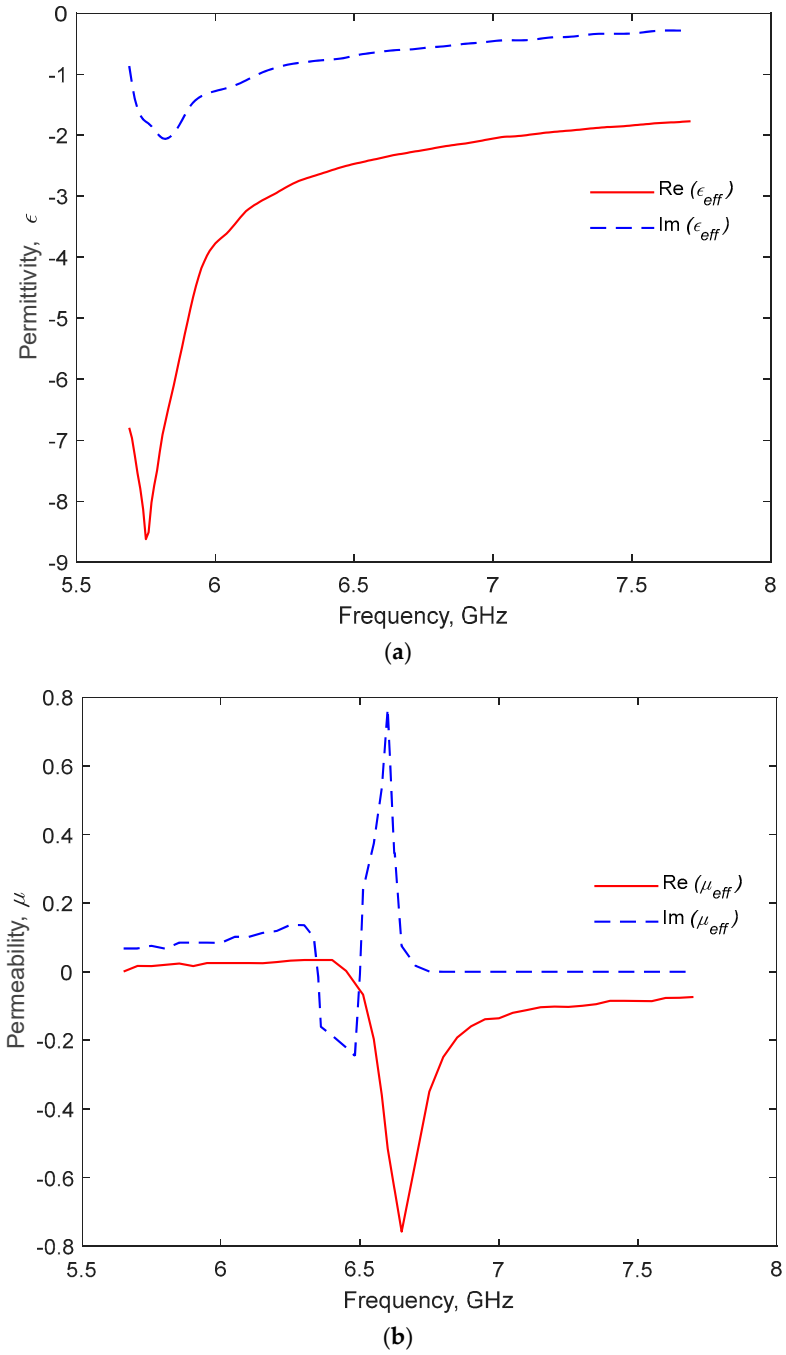

Figure 4. Analysis of the MTM second layer according to the values of ε and μ: (**a**) permittivity; (**b**) permeability.

Consequently, the integration of this MTM-based layer, which is fabricated on a Rogers RO4003C substrate with a thickness of h = 0.204 mm (approximately 8 mils), not only enhances the gain but also significantly improves the isolation between adjacent antenna elements, reducing mutual coupling and interference. These attributes make the proposed design highly suitable for advanced MIMO systems in 5G communications, where compactness, high efficiency, and robust performance are paramount. The ability to manipulate phase velocity and wavefront curvature through the DNG properties of the MTM layer further underscores its potential for next-generation wireless systems.

3. Results and Discussion

This section includes both a summary of the main results and the characteristics of the design of the antenna, along with a subsection devoted to presenting the prototype produced and the results of the return loss measurements.

3.1. Antenna Performance

This subsection includes the main results of the simulations carried out using the CST software. First of all, and according to the antenna layout presented in Figure 1, it must be pointed out that each antenna element is oriented in different directions, ensuring comprehensive coverage across all angular directions.

Let us start the analysis by looking at the mutual coupling between antennas. In this sense, Figure 5 presents the mutual coupling between the antenna elements, showing values lower than −18 dB, indicating strong isolation between the antenna elements and minimal interference, which are crucial for maintaining high MIMO performance. The 2D and 3D radiation patterns are illustrated in Figures 6 and 7, respectively, providing a comparative analysis of the antenna's performance with and without the incorporation of metamaterials. Specifically, Figures 6a and 7a represent the radiation pattern of the antenna in the absence of the CRR layer, whereas Figures 6b and 7b depict the radiation pattern when the CRR layer is integrated. A comparison of these results clearly demonstrates that the inclusion of MTM enhances the antenna's radiation characteristics and directionality. The observed improvement in uniform coverage in Figure 6b further validates the effectiveness of MTM in optimizing the antenna's radiation performance. The envelope correlation coefficient (ECC) values, provided in Figure 8, are consistently below 0.025, signifying the excellent isolation and minimal mutual coupling between the antenna elements, which contributes to the high performance of the MIMO system. Due to the symmetry of the antenna design, both mutual coupling and ECC values have been presented, taking antenna element 1 as a reference as the results are identical in the rest of the situations.

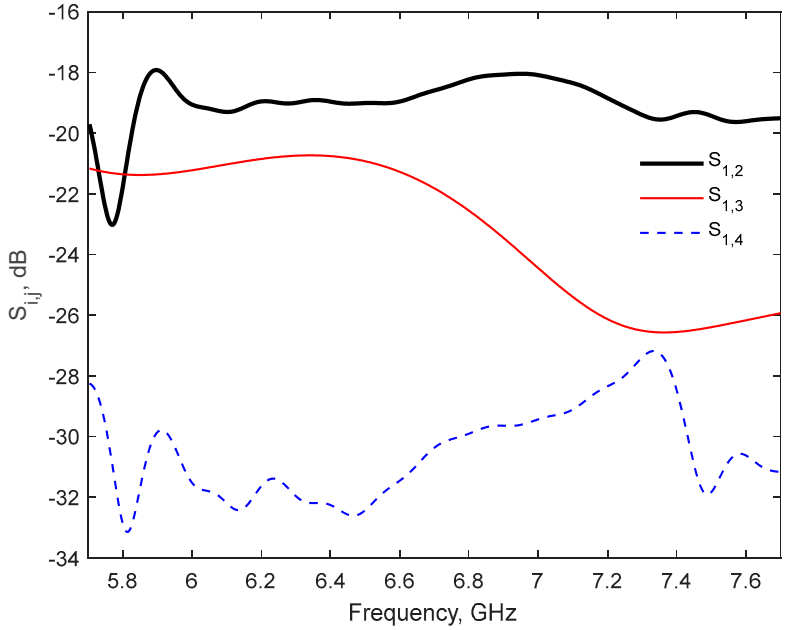

Figure 5. Mutual coupling between antenna elements. Antenna element 1 (port 1) has been considered as reference.

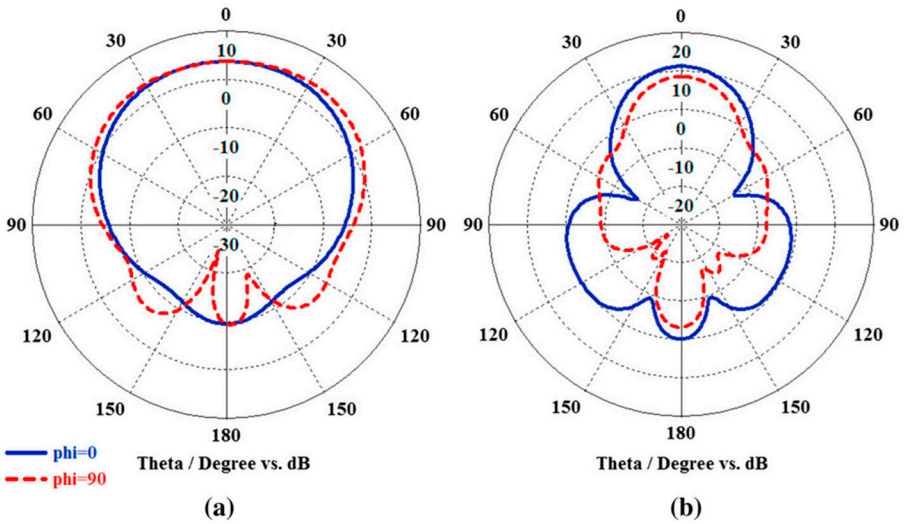

Figure 6. Radiation patterns of antenna for $\phi = 0^\circ$ and $\phi = 90^\circ$ cuts: (**a**) without MTM layer; (**b**) with MTM layer.

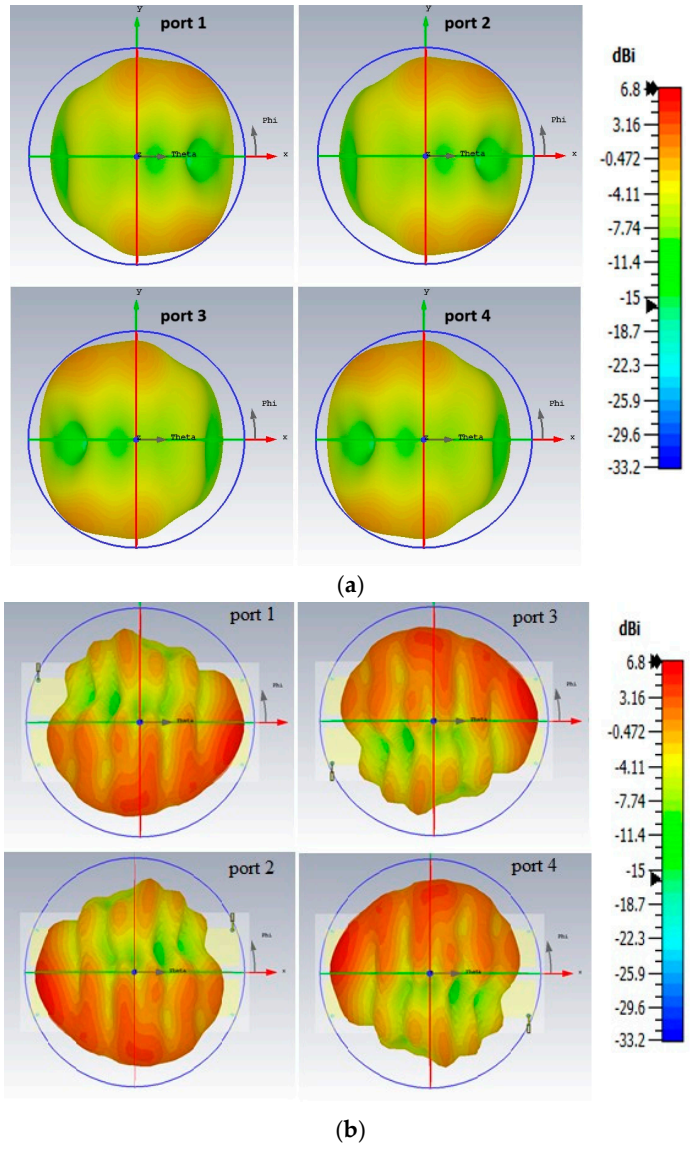

Figure 7. Three-dimensional radiation patterns of proposed antenna system: (**a**) without CRR; (**b**) with CRR.

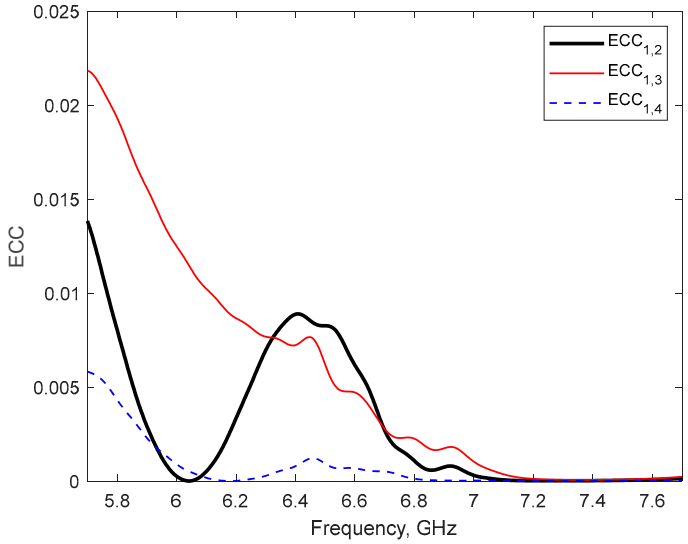

Figure 8. Values of the envelope correlation coefficient, ECC. Antenna element 1 (port 1) has been considered as a reference.

Furthermore, Figure 9 presents the antenna's efficiency, which exceeds 75% across the operating band, with a peak efficiency of 81%, ensuring reliable signal transmission. The results show clearly the usefulness and improvement achieved when introducing the CRR structure, as the initial antenna design with no MTM leads to a far lower efficiency, ranging from 69.1% to 74.2% across the entire 6425–7125 MHz frequency band of interest.

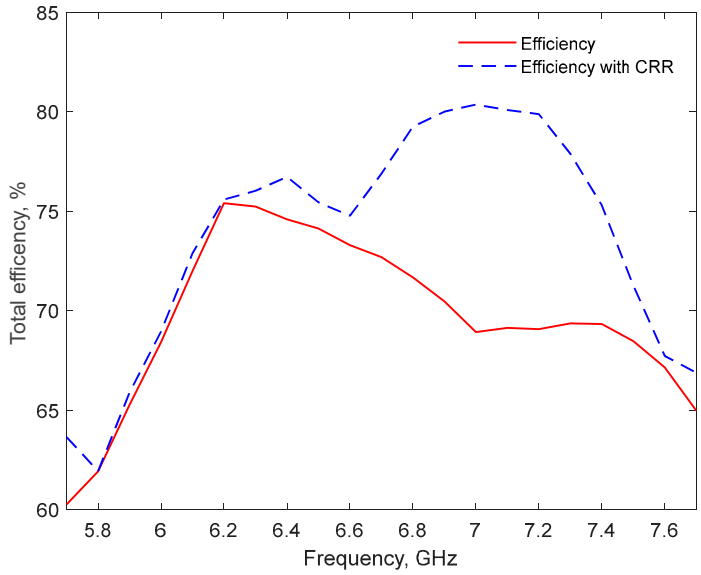

Figure 9. Total efficiency of the antenna system, showing the effect of the MTM layer.

Finally, Figure 10 shows a comparison of the gain of the proposed MIMO system with and without the CRR-based metamaterial layer. The CRR layer enhances the gain significantly, by at least 1.5 dB across the entire bandwidth, confirming the effectiveness of the MTM in boosting the antenna's performance, especially in the FR1 band and mmWave spectrum, which are critical for 5G communications.

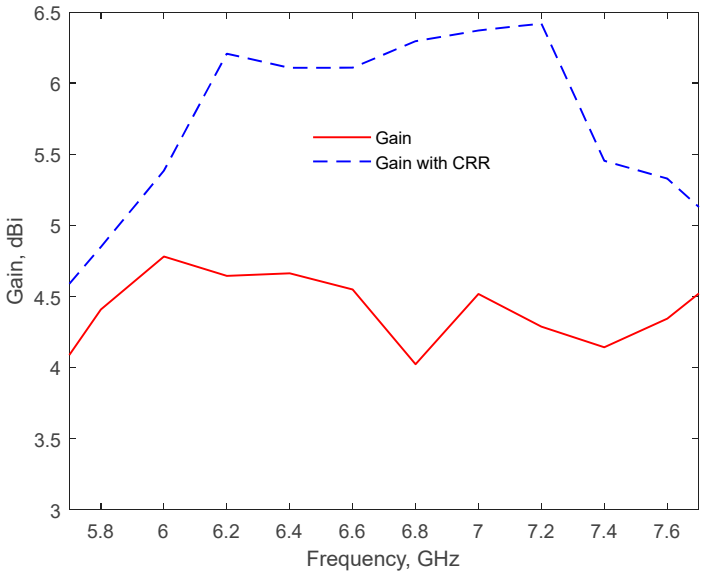

Figure 10. Antenna gain, including the effect of the MTM layer.

3.2. Antenna Prototype and Measurements

The prototype of the 2 × 2 antenna array is shown in Figure 11.

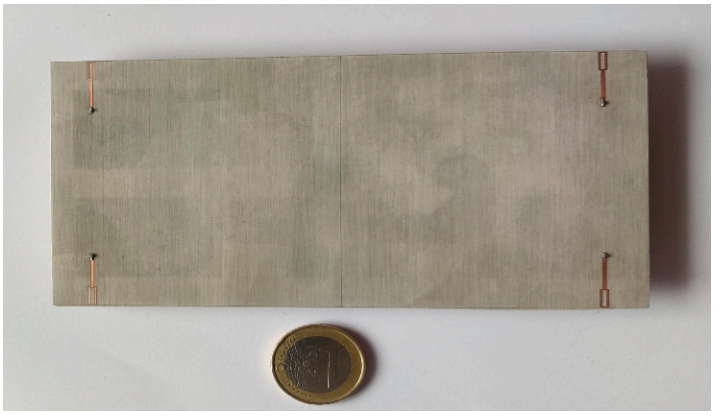

(**a**)

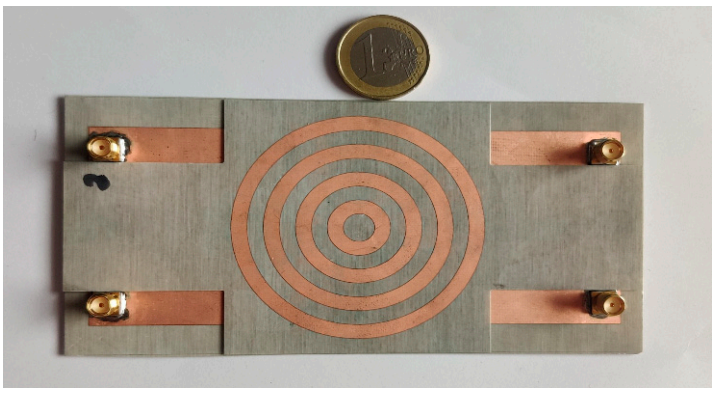

(**b**)

Figure 11. Antenna prototype: (**a**) top view of the MIMO antenna; (**b**) back view of the MIMO antenna, including the CRR-based MTM structure placed on top.

The measurements of the antenna have been carried out in a small-sized anechoic facility available at the University of Cantabria, using the P5006A 2-Port vectorial network

analyzer (VNA) from Keysight Technologies (Santa Rosa, CA, USA). The details of the measurement setup are shown in Figure 12.

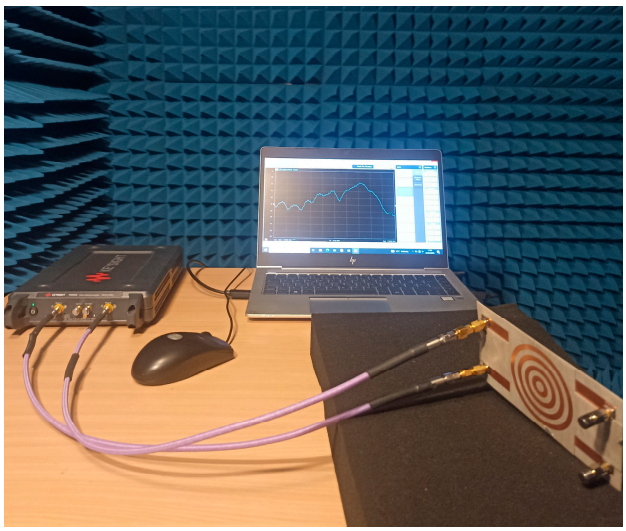

Figure 12. Measurement setup. Details of the configuration for mutual coupling analysis.

The reflection coefficient, i.e., the S_{ii} parameter for any of the ports (i = 1 to 4), has been measured in a small-sized anechoic facility available at the University of Cantabria using the 2-Port P5006A VNA properly calibrated in the 5.7–7.7 GHz frequency range. Representative results for the antenna port 1 are presented in Figure 13, and a similar performance is appreciated for the rest of the ports. The comparison between the simulations and measurements demonstrates a good agreement between the antenna design and the prototype, thus confirming the accuracy of the antenna design proposed. The differences observed between the simulations and measurements are related to different factors influencing the manufacturing of the prototype, including differences or tolerances in the substrate properties, discontinuities at the feeding ports and connectors, along with parasitic effects. Moreover, focusing on the measurements of the prototype, it can be inferred from Figure 13 that the return losses are higher than 15.5 dB in the frequency band of interest, i.e., 6.425–7.125 GHz.

In order to analyze the performance of the fabricated antenna prototype in terms of the mutual coupling between the antenna elements, and to validate the results of the simulations presented in Figure 5, Figure 14 shows the associated measured mutual coupling values. The results show a strong isolation between the antenna elements, even higher than that obtained in the simulations, i.e., the measured values are lower than −21.7 dB against the −18 dB appreciated in Figure 5 for the simulations.

Finally, to show the effectiveness of the proposed antenna, a comprehensive comparative analysis with other previously published works is presented in Table 2. It must be pointed out that most of the results in [22–28] are intended for a different frequency band, but have been used as a reference to show their agreement with this proposal. Apart from the technical data, the summary in Table 2 also includes a column indicating the designs that incorporate metal rim structures, along with an additional column, i.e., the decoupling method column, to specify, in this case, the techniques used in each work to reduce the mutual coupling between antenna elements, a crucial matter in MIMO performance evaluation.

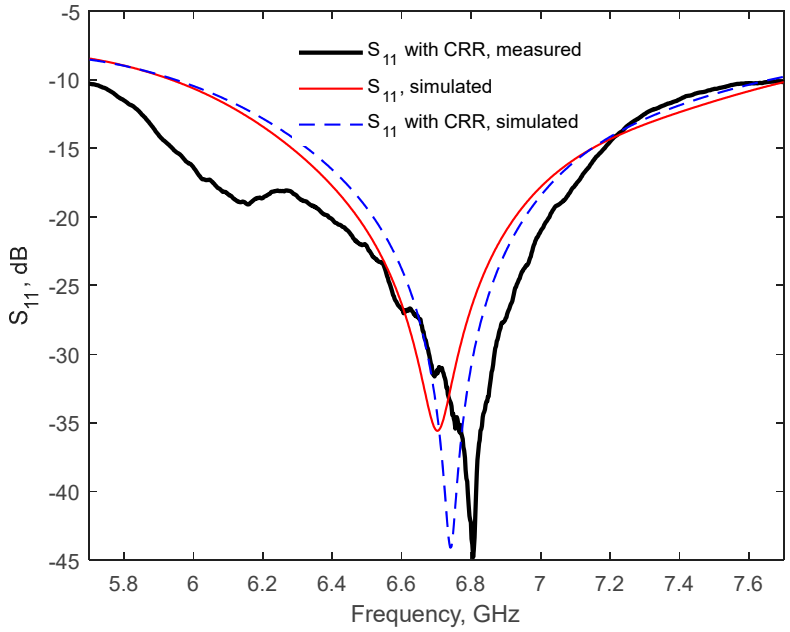

Figure 13. The S_{11} parameter for port 1, considered as a reference. The results include the S_{11} for the initial antenna, the associated S_{11} when introducing the MTM layer (both obtained from simulations), and the measurement results for the complete fabricated prototype, including the MTM layer.

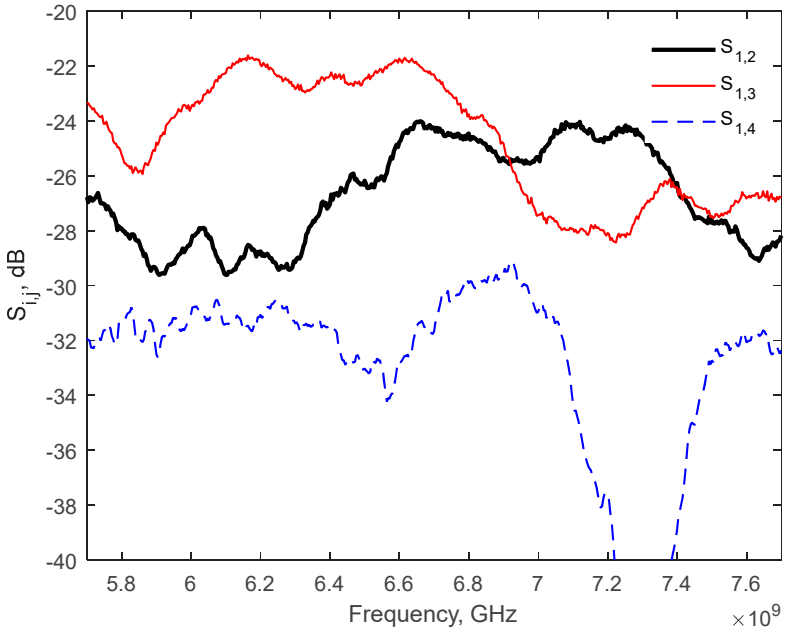

Figure 14. The results of the mutual coupling between the antenna elements of the prototype. Antenna element 1 (port 1) has been considered as a reference.

Table 2. Comparative analysis with previous studies.

Reference	Bandwidth (GHz)	Metal Rim	Isolation (−dB)	ECC	Decoupling Method	T. Efficiency (%)
[22]	5.0–5.8	No	>20	<0.04	Radiation direction diversity	51–89
[23]	3.29–6.61	No	>16.6	<0.057	Meander line DGS	53–86
[24]	4.4–5.0	Yes	>11.5	<0.2	Spatial diversity	38–52
[25]	3.3–5.95	Yes	>15	<0.11	Connecting line	47–78

Table 2. *Cont.*

Reference	Bandwidth (GHz)	Metal Rim	Isolation (−dB)	ECC	Decoupling Method	T. Efficiency (%)
[26]	3.4–3.6 5.4–5.6	No	>13	<0.1	Rectangular DGS	52–58
[27]	3.3–6.0	Yes	>18	<0.04	Neutral line	40–60
[28]	3.3–7.1	Yes	>11	<0.09	-	47–70
Proposed	6.4–7.1	No	>18	<0.025	MTM+DGS	75–81

3.3. Intended Practical Application of the Antenna: Integration in a Channel Sounder

Concerning IMT systems moving towards 2030 and beyond (IMT-2030), the development of efficient and reliable channel models will contribute to the development of upcoming 6G mobile networks. In this sense, novel and improved channel sounders are required to contribute to a more realistic experimental characterization of the radio channel. In order to improve the channel sounder previously developed for mMIMO (both concentrated and distributed) channel characterization [18,19], the antenna prototype will be included as a key element of the channel sounder to be developed, shown in Figure 15.

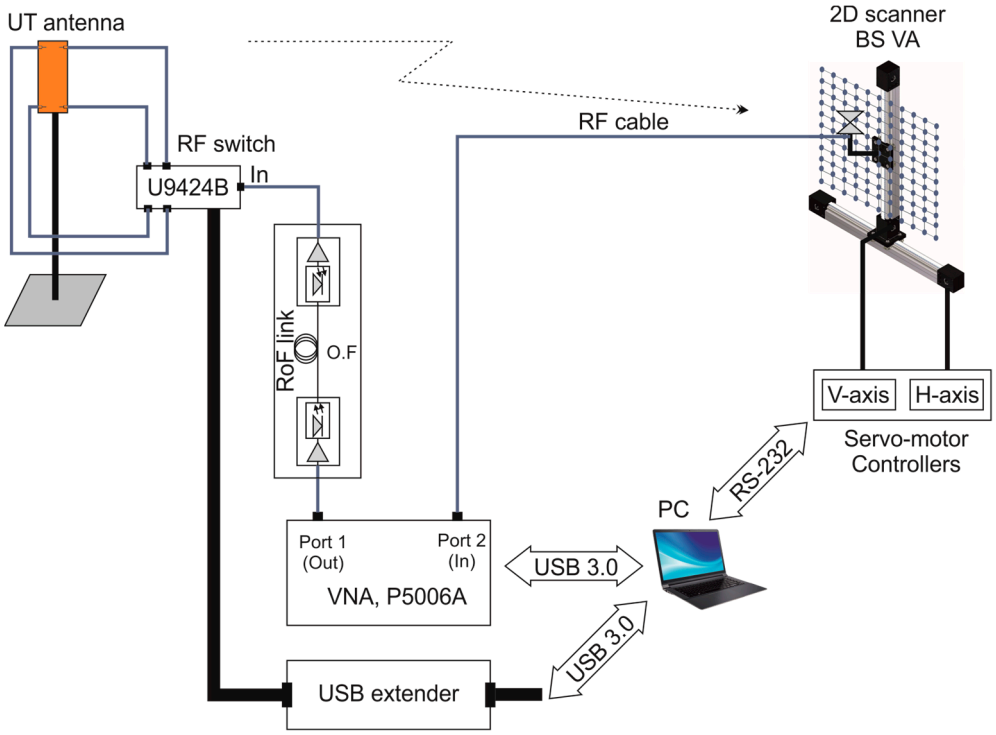

Figure 15. Block diagram of the improved channel sounder proposed.

The channel sounder presented in Figure 15 introduces significant changes to that which is already used by the authors in [18,19]. Basically, in order to mimic the mMIMO array at the base station (BS), it consists of a 2D planar scanner array that, being remotely controlled, makes it possible to move the receiver (Rx) antenna implementing a virtual array (VA). On the transmitter (Tx) side, representing the position of a hypothetical UT, the antenna prototype presented in this paper in combination with a radio frequency (RF) switch will make it possible to emulate a virtual 2 × 2 MIMO array, so that for every connected port of the switch, the Tx-Rx radio channel can be measured. For this purpose, the P50006A VNA from Keysight Technologies (Santa Rosa, CA, USA). is used to measure in the frequency domain the $S_{21}(f)$ scattering parameter, representing the complex channel

transfer function established between the *i*-th port of the UT's antenna and the *k*-th point of the VA at the BS. The 2D planar scanner, the VNA, along with the RF switch, are all remote-controlled from a computer in order to synchronize VA movements, UT antenna port excitation, along with the acquisition of the associated *S*-trace. Finally, the amplified RoF link makes it possible to mitigate the high losses of the channel, increasing the dynamic range in the measurement, thus making it possible to increase the distance between the Tx and Rx antennas. In short, the introduction of this antenna prototype in the channel sounder will make it possible to carry out channel measurements in a more realistic fashion and over larger areas.

4. Conclusions

This work presents the development of a compact, high-performance, 2×2 MIMO antenna system optimized for operation in the 6425–7125 MHz frequency band, addressing the key challenges of antenna integration and gain enhancement for 5G mobile devices. The design incorporates a metamaterial-based CRR layer to improve antenna gain by at least 1.5 dB across the entire bandwidth, demonstrating its effectiveness in mitigating path loss associated with the increasingly higher frequency bands proposed for 5G systems and beyond. The antenna has been fabricated, and the measurements of the prototype are close to those obtained with the simulations, validating the accuracy and reliability of the design. The antenna presented provides excellent isolation (mutual coupling below -18 dB), low envelope correlation coefficients (ECC < 0.025), along with an efficiency exceeding 75%. These results, combined with the uniform radiation patterns and comprehensive directional coverage, confirm the robustness and suitability of the proposed MIMO system for 5G communication applications in mobile devices. In fact, the antenna prototype will be included in the future as a key part of a channel sounder to solve channel characterization issues in a more realistic fashion. Future work will focus on exploring reconfigurable metamaterial structures for adaptive frequency operations and extending the current design principles to mmWave bands for upcoming 6G applications.

Author Contributions: Conceptualization, A.G., A.T., J.T. and R.P.T.; methodology, A.G., A.T. and J.R.P.; software, A.G. and J.R.P.; validation, A.G., J.R.P., R.P.T., A.T. and J.T.; formal analysis, A.G., A.T., J.T. and R.P.T.; investigation, A.G., J.R.P. and A.T.; data curation, A.G. and J.R.P.; writing—review and editing, A.G., J.R.P., R.P.T., A.T. and J.T.; visualization, A.G. and J.R.P.; funding acquisition, J.R.P. and R.P.T. All authors have read and agreed to the published version of the manuscript.

Funding: This work has been supported by the MCIN/AEI/10.13039/501100011 033/ through the I+D+i Project under Grant PID2020-119173RB-C22, and the Contrato Programa Gobierno de Cantabria-UC under the Proyectos Puente 2024 funds (12.VP96.64662).

Data Availability Statement: Data are contained within the article.

Acknowledgments: The authors would like to thank Eva M. Cuerno and Paul García, technicians in the Circuit Technology Laboratory of the Department of Communications Engineering at the Universidad de Cantabria, for their support with the fabrication of the antenna prototype.

Conflicts of Interest: The authors declare no conflicts of interest. The funders had no role in the design of the study; in the collection, analysis, or interpretation of the data; in the writing of the manuscript; or in the decision to publish the results.

Abbreviations

The following abbreviations are used in this manuscript:

2D	Two-dimensional
3D	Three-dimensional
5G	Fifth-generation
6G	Sixth-generation
AMC	Artificial magnetic conductor
BS	Base station
CRR	Concentric rings resonator
DNG	Double-negative
DGS	Defective ground structure
DPS	Double-positive
EBG	Electromagnetic bandgap
ECC	Envelope correlation coefficient
ENG	Epsilon-negative
EMW	Electromagnetic wave
FR1	Frequency range 1
FSS	Frequency selective surface
IMT	International mobile telecommunications
ITU	International telecommunication union
LHMs	Left-handed materials
MIMO	Multiple-input multiple-output
mMIMO	Massive multiple-input multiple-output
mmWave	Millimeter-wave
MNG	Mu-negative
MTM	Metamaterial
NIM	Negative-index metamaterial
PRS	Partially reflecting surface
RF	Radio frequency
RIS	Reconfigurable intelligent surfaces
RoF	Radio-over-fiber
Rx	Receiver
SRR	Split-ring resonator
Tx	Transmitter
UT	User terminal
UWB	Ultra-wideband
VA	Virtual array
VNA	Vector network analyzer
WRC	World Radio Communication Conference

References

1. Final Acts WRC-23. Available online: https://www.itu.int/hub/publication/r-act-wrc-16-2024/#/en (accessed on 12 March 2025).
2. Guariglia, E. Entropy and fractal antennas. *Entropy* **2016**, *18*, 84. [CrossRef]
3. Krzysztofik, W.J. Fractal geometry in electromagnetics applications—From antenna to metamaterials. *Microw. Rev.* **2013**, *19*, 3–14.
4. Haider, A.; Rahman, M.U.; Ahmad, H.; NaghshvarianJahromi, M.; Niaz, M.T.; Kim, H.S. Frequency-agile WLAN notch UWB antenna for URLLC applications. *Comput. Mater. Contin.* **2021**, *67*, 2243–2254. [CrossRef]
5. Al-Gburi, A.J.A.; Ibrahim, I.-M.; Zakaria, Z.; Zeain, M.Y.; Alwareth, H.; Ibrahim, A.M.; Keriee, H.H. High gain of UWB CPW-fed mercedes-shaped printed monopole antennas for UWB applications. *Przegląd Elektrotechniczny* **2021**, *97*, 70–73. [CrossRef]
6. Zeain, M.Y.; Abu, M.; Althuwayb, A.A.; Alsariera, H.; Al-Gburi, A.J.A.; Abdulbari, A.A.; Zakaria, Z. A new technique of FSS-based novel chair-shaped compact MIMO antenna to enhance the gain for sub-6GHz 5G applications. *IEEE Access* **2024**, *12*, 49489–49507. [CrossRef]

7. Varshney, A.; Gençoğlu, D.N. High-gain multi-band Koch fractal FSS antenna for sub-6 GHz applications. *Appl. Sci.* **2024**, *14*, 9022. [CrossRef]
8. Qin, Y.; Wang, P.; Wang, Y.; Yan, Z. Wideband Fabry-Perot cavity antenna based on single layer partially reflective surface with multiple resonances. *IEEE Antennas Wirel. Propag. Lett.* **2024**, *23*, 4688–4692. [CrossRef]
9. Li, Q.; Liao, S.; Yang, Y.; Liang, Z.; Xiao, S. Wideband 5G millimeter-wave MIMO magneto-electric dipole antenna integrated with partially reflective surfaces. *IEEE Trans. Antennas Propag.* **2023**, *72*, 445–453. [CrossRef]
10. Deng, F.; Luk, K.M. A wideband spherical Fabry–Perot cavity antenna based on positive phase gradient metasurface. *IEEE Trans. Antennas Propag.* **2023**, *71*, 5558–5565. [CrossRef]
11. Lin, X.; Seet, B.-C.; Joseph, F.; Li, E. Flexible fractal electromagnetic bandgap for millimeter-wave wearable antennas. *IEEE Antennas Wirel. Propag. Lett.* **2018**, *17*, 1281–1285. [CrossRef]
12. Jin, C.; Chen, J.; Zhang, B.; Kong, L.; An, S.; He, Z.S.; Liu, J. Low-cost mmWave metallic waveguide based on multilayer integrated vertical-EBG structure and its application to slot array antenna design. *IEEE Trans. Antennas Propag.* **2021**, *70*, 2205–2213. [CrossRef]
13. Kumari, P.; Gangwar, R.K.; Chaudhary, R.K. An aperture-coupled stepped dielectric resonator UWB MIMO antenna with AMC. *IEEE Antennas Wirel. Propag. Lett.* **2022**, *21*, 2040–2044. [CrossRef]
14. Yang, S.; Liang, L.; Wang, W.; Fang, Z.; Zheng, Y. Wideband gain enhancement of an AMC cavity-backed dual-polarized antenna. *IEEE Trans. Veh. Technol.* **2021**, *70*, 12703–12712. [CrossRef]
15. Puneeth Kumar, T.R.; Karthik, R.; Krishnamoorthy, K. A zero-index based metasurface antenna with improved gain and circular polarization characteristics. In Proceedings of the 2021 IEEE Texas Symposium on Wireless and Microwave Circuits and Systems (WMCS), Waco, TX, USA, 1–2 April 2021. [CrossRef]
16. Saleh, C.M.; Almajali, E.; Jarndal, A.; Yousaf, J.; Alja'Afreh, S.S.; Amaya, R.E. Wideband 5G antenna gain enhancement using a compact single-layer millimeter wave metamaterial lens. *IEEE Access* **2023**, *11*, 14928–14942. [CrossRef]
17. Rajanna, P.K.T.; Rudramuni, K.; Kandasamy, K. A high-gain circularly polarized antenna using zero-index metamaterial. *IEEE Antennas Wirel. Propag. Lett.* **2019**, *18*, 1129–1133. [CrossRef]
18. Pérez, J.R.; Torres, R.P.; Domingo, M.; Valle, L.; Basterrechea, J. Analysis of massive MIMO performance in an indoor picocell with high number of users. *IEEE Access* **2020**, *8*, 107025–107034. [CrossRef]
19. Pérez, J.R.; Fernández, Ó.; Valle, L.; Bedoui, A.; Et-tolba, M.; Torres, R.P. Experimental analysis of concentrated versus distributed massive MIMO in an indoor cell at 3.5 GHz. *Electronics* **2021**, *10*, 1646. [CrossRef]
20. Zabo, Z.; Park, G.H.; Hedge, R.; Li, E.-P. A unique extraction of metamaterial parameters based on Kramers-Kronig relationship. *IEEE Trans. Microw. Theory Technol.* **2010**, *58*, 2646–2653. [CrossRef]
21. Ashraf, F.B.; Alam, T.; Islam, M.T. A uniplanar left-handed metamaterial for terrestrial microwave links. *IEEE Microw. Wirel. Compon. Lett* **2018**, *28*, 108–110. [CrossRef]
22. Hu, Y.; Wang, Y.; Zhang, L.; Li, M. Design of Miniaturized and Wideband Four-Port MIMO Antenna Pair for WiFi. *Micromachines* **2024**, *15*, 850. [CrossRef]
23. Dey, S.; Dey, S. Wideband highly efficient eight element MIMO antenna using differential fed open end slot for sub-7 GHz 5G mobile handset applications. *IEEE Trans. Circuits Syst. II Express Briefs* **2024**, *78*, 3760–3764. [CrossRef]
24. Ahn, J.; Youn, Y.; Kim, B.; Lee, J.; Choi, N.; Lee, Y.; Kim, G.; Hong, W. Wideband 5G N77/N79 4 × 4 MIMO antenna featuring open and closed stubs for metal-rimmed smartphones with four slits. *IEEE Antennas Wirel. Propag. Lett.* **2023**, *22*, 2798–2802. [CrossRef]
25. Sun, L.; Li, Y.; Zhang, Z. Wideband decoupling of integrated slot antenna pairs for 5G smartphones. *IEEE Trans. Antennas Propag.* **2020**, *69*, 2386–2391. [CrossRef]
26. Ali, H.; Ren, X.-C.; Hashmi, A.M.; Anjum, M.R.; Bari, I.; Majid, S.I.; Jan, N.; Tareen, W.U.K.; Iqbal, A.; Khan, M.A. An eight element dual band antenna for future 5G smartphones. *Electronics* **2021**, *10*, 3022. [CrossRef]
27. Chen, Y.T.; Su, H.L. A Sub-6 GHz 8 × 8 MIMO Antenna Array for 5G Metal-Frame Mobile Phone Applications. *Electronics* **2024**, *13*, 4590. [CrossRef]
28. Cai, Q.; Li, Y.; Zhang, X.; Shen, W. Wideband MIMO antenna array covering 3.3–7.1 GHz for 5G metal-rimmed smartphone applications. *IEEE Access* **2019**, *7*, 142070–142084. [CrossRef]